coatings

MDPI

Article

Corrosion Resistance of Ti Coatings, Cr Coatings, and Ti/Cr Multilayer Coatings Prepared on 7050 Aluminum Alloy by Magnetron Sputtering

Kang Chen [1], Tao He [1,*], Xiangyang Du [1], Artem Okulov [2], Catherine Sotova [3], Yang Ding [1], Yuqi Wang [1] and Peiyu He [1]

[1] School of Mechanical and Automotive Engineering, Shanghai University of Engineering Science, Shanghai 201600, China; ck1714131870@163.com (K.C.)
[2] M.N. Mikheev Institute of Metal Physics, Ural Branch of the Russian Academy of Sciences, Ekaterinburg 620108, Russia
[3] Department of High-Efficiency Machining Technologies, Moscow State University of Technology "STANKIN", Moscow 127055, Russia
* Correspondence: hetao@sues.edu.cn

Abstract

Al7050 aluminum alloy substrates were coated with Cr, Ti, and Ti/Cr multilayer films via direct current magnetron sputtering to enhance their corrosion resistance. A comprehensive analysis, employing SEM and XRD, characterized the coatings' morphology and composition, while electrochemical experiments assessed their corrosion performance. The Cr coating, despite exhibiting the largest thickness (588 nm), revealed a porous microstructure with inherent structural weaknesses. Conversely, the Ti coating, while possessing a dense structure, presented a significantly reduced thickness (96 nm). The Ti/Cr multilayer coating, with a thickness of 242 nm, achieved an optimal balance between structural density and overall thickness. Critically, the layered architecture of the Ti/Cr multilayer coating effectively impeded crack propagation and facilitated the formation of tortuous corrosion pathways. This intricate pathway morphology significantly hindered the diffusion of the corrosive medium, resulting in a notably low corrosion current density of 3.83×10^{-7} A·cm^{-2}. Comparative analysis revealed that the corrosion current density of the Ti/Cr multilayer coating was substantially lower than that of both the Cr and Ti coatings, demonstrating improvements of 2386% and 222%, respectively. These findings underscore the pivotal role of the multilayer structure in augmenting the corrosion resistance of aluminum alloys by providing a superior barrier to corrosive medium.

Keywords: multilayer coating; corrosion resistance; aluminum alloy; magnetron sputtering

check for updates

Academic Editor: Víctor Orozco Carmona

Received: 12 August 2025
Revised: 7 September 2025
Accepted: 12 September 2025
Published: 14 September 2025

Citation: Chen, K.; He, T.; Du, X.; Okulov, A.; Sotova, C.; Ding, Y.; Wang, Y.; He, P. Corrosion Resistance of Ti Coatings, Cr Coatings, and Ti/Cr Multilayer Coatings Prepared on 7050 Aluminum Alloy by Magnetron Sputtering. *Coatings* **2025**, *15*, 1077. https://doi.org/10.3390/coatings15091077

Copyright: © 2025 by the authors. Licensee MDPI, Basel, Switzerland. This article is an open access article distributed under the terms and conditions of the Creative Commons Attribution (CC BY) license (https://creativecommons.org/licenses/by/4.0/).

1. Introduction

Aluminum and aluminum alloys have garnered increasing attention due to their low density, high strength-to-weight ratio, and excellent thermal conductivity. With their superior mechanical properties, relatively low production and processing costs, and good recyclability, they have taken a leading position in the production and manufacturing of various products [1,2]. However, corrosion of aluminum alloys is the primary mode of equipment failure, with the economic costs resulting from material corrosion damage estimated at approximately 3–5% of annual gross domestic product [3]. Therefore, there is a need to find a solution that provides excellent corrosion protection for aluminum alloys

under harsh working conditions. Many researchers have explored various methods, such as adding rare earth elements to aluminum alloys, multi-stage aging treatment, and severe plastic deformation to enhance corrosion resistance [4–6]. Coating technology has been proven to be one of the most effective methods for extending the service life and reliability of metal alloys parts. It achieves this by depositing corrosion-resistant coatings that isolate the substrate from corrosive media without altering the substrate's properties [7,8]. As a result, various protective coatings are widely used in industries such as automotive manufacturing, marine engineering, aerospace, and other.

Coatings prepared by physical vapor deposition (PVD) are widely used due to their compact structure, uniform composition, and low roughness [9]. Among these, Cr coatings have been proven to effectively enhance the service life and reliability of metal parts made of steel and various alloys by protecting them from chemical corrosion and increasing their wear resistance [10–12]; Ti coatings, with their excellent mechanical properties and superior corrosion resistance (forming a robust protective oxide layer on the metal surface), are widely applied for protecting critical components in corrosive environments [13–15]. However, despite the many superior properties of Ti coatings and Cr coatings, structural defects (such as pores and cracks) caused by the continuous growth of columnar crystals during coating process often allow corrosive media (such as Cl^- and SO_4^{2-}) to penetrate the substrate, thereby reducing the corrosion resistance of the protected parts [16,17]. To overcome these defects, researchers have attempted to develop multilayer coatings to achieve reliable corrosion resistance and reduce interfacial contact resistance. Multilayer coatings can exhibit layered interfaces parallel to the coating surface within the coating structure, overcoming most coating defects and providing the coating with high corrosion resistance [18]. Liu et al. [19] compared the structure and corrosion behavior of VN coatings and multi-layer VN/C coatings prepared on 316L steel via PVD. They found that the C nanolayer disrupted the growth of large grains in the VN layer, thereby enhancing coating toughness and suppressing crack initiation, while the nano-multi-layer structure hindered the penetration of corrosive media. Onur [20] prepared TiN, TiAlN coatings, and TiAlN/TiN multilayer coatings on the surface of Ti45Nb and analyzed their corrosion resistance. The results showed that compared to single-layer coatings, multilayer coatings have finer grain sizes and more stable coating structures, thereby improving corrosion resistance. Additionally, the wetting characteristics of different coating surfaces also influence corrosion resistance. Xie et al. [21] deposited AlN coatings and $(Al/AlN)_5$ multilayer coatings on AZ31 magnesium alloy and analyzed their corrosion resistance. The superior corrosion resistance of the multilayer coatings was attributed to their denser layered structure, better crack propagation resistance, and deformation coordination between the coating and substrate during corrosion.

While multilayer coatings have demonstrated effectiveness in enhancing the corrosion resistance of materials like steel, titanium, and magnesium alloys, a comprehensive comparison of Cr, Ti, and Ti/Cr multilayer coatings applied directly to aluminum alloy substrates remains limited. Addressing this gap, the present study employs direct current magnetron sputtering to deposit Ti, Cr, and Ti/Cr multilayer coatings onto 7050 aluminum alloy. This research investigates the structural characteristics and corrosion protective behavior of these coatings in 3.5% NaCl solution environment. Furthermore, by analyzing electrochemical mechanisms, the study aims to elucidate the corrosion evolution process and detailed corrosion mechanisms associated with each coating type—Ti, Cr, and the Ti/Cr multilayer configuration—providing a deeper understanding of their respective strengths and weaknesses in protecting aluminum alloys from corrosion. This in-depth analysis will contribute to the development of optimized coating strategies for aluminum alloys in harsh marine environments.

2. Materials and Methods

2.1. Substrate Preparation

A sample made of 7050 aluminum alloy (Southwest Aluminium (Group) Co., Ltd., Chongqing, China) with dimensions of Ø28 mm × 3 mm was used as the substrate. The substrate was progressively ground using SiC sandpaper with grit sizes ranging from #400 to #2000, followed by mechanical polishing with diamond slurry. Subsequently, the substrate samples were ultrasonically cleaned with 99.5% acetone for 10 min. It is worth noting that, to characterize the microstructure of the coating more efficiently, silicon wafers (P-type, crystal orientation (100), resistivity <0.02 ohm) were also used for coating preparation, with the same deposition conditions as the aluminum substrate.

2.2. Coating Deposition

A direct current magnetron sputtering system (MSP-300C, Beijing Chuangshi Weina Technology Co., Ltd., Beijing, China) was used to deposit the coating on silicon wafers and on aluminum substrates that have been ground and polished. The system's base vacuum level is set to 8×10^{-4} Pa, followed by the introduction of high-purity Ar gas to maintain a pressure of 0.3 Pa. The deposition is performed at room temperature by controlling the system to sputter a high-purity Ti target (99.995%, ZhongNuo Advanced Material, Beijing, China) and Cr target (99.995%, ZhongNuo Advanced Material, Beijing, China). Both the Ti target and Cr target operate at a power of 200 W. Prior to coating deposition, each target is cleaned via argon ion sputtering for 10 min. Due to the differing sputtering rates of the Cr target and Ti target, the deposition times of the two targets are controlled to prepare Cr coatings, Ti coatings, and Ti/Cr multilayer coatings. The total deposition time for all three coatings was 80 min. Previous experiments have demonstrated that under similar sputtering conditions, the sputtering rates of Ti and Cr targets are approximately one-third of each other [22]. To avoid the influence of sublayer thickness in multilayer coatings, the Ti/Cr multilayer coating was prepared by alternately sputtering the Ti target (15 min) and Cr target (5 min) four times using a shutter system, with the outermost layer being the Cr coating.

2.3. Microstructural Characterization

The phase composition of the coated silicon wafer samples was examined using GIXRD analysis with a D/max-2500/PC diffractometer (DMAX-RB, Rigaku Corporation, Tokyo, Japan) equipped with Cu Kα radiation. The incident angle was 0.25°, the step size was 0.02°, the scanning speed was 4°/min, and the 2θ range was 20–90°. The surface morphology of coated aluminum alloy samples before and after corrosion, as well as the morphology and thickness of the cross-section of coated silicon wafer samples, were observed using a scanning electron microscope (SEM) equipped with energy-dispersive spectroscopy (EDS) (Hitachi SU5000, Tokyo, Japan).

2.4. Corrosion Resistance Study

At room temperature, the electrochemical performance of uncoated, Cr-coated, Ti-coated, and Ti/Cr multilayer-coated aluminum alloys was tested using a three-electrode electrochemical system (CHI 760D, Shanghai Chenhua Instrument Co., Ltd., Shanghai, China). A standard calomel electrode was used as the reference electrode, a platinum electrode as the counter electrode, and the coated samples as the working electrode, with an exposed area of 1 cm^2. First, the coated samples were immersed in a 3.5 wt.% NaCl solution for 30 min to ensure the test system was in equilibrium. Then, the impedance spectra of the samples were measured using a sinusoidal alternating signal with an amplitude of 10 mV as the excitation signal. The test frequency range is 10^{-2} to 10^5 Hz. After the impedance test, a dynamic potential polarization test is performed at a scan rate of 1.0 mV/s within the

voltage range of −1.2 V to +1.2 V. For aluminum alloy, the dynamic potential polarization test is conducted at a scan rate of 1.0 mV/s within the voltage range of −2 V to 0 V. Each sample underwent three separate experiments to ensure experimental reproducibility.

3. Results

3.1. Coating Phase Structure

Figure 1 shows the XRD patterns of the coatings deposited on the Si substrate. The XRD analysis results indicate that the Cr coating exhibits (110) crystal plane preferential orientation, belonging to the body-centered cubic (BCC) structure; while the Ti coating exhibits (101) crystal plane preferential orientation, belonging to the hexagonal close-packed (HCP) structure. In the Ti/Cr multilayer coating, both Ti(101) and Cr(110) crystal plane-corresponding diffraction peaks were observed, indicating the coexistence of two-phase crystal structures in the multilayer structure [23]. Notably, all coating samples exhibit a shift in diffraction peaks toward higher angles, a phenomenon primarily attributed to internal stresses introduced during high-power magnetron sputtering, which cause lattice compression in the coating, reducing interplanar spacing and resulting in the shift in diffraction peaks toward higher angles [24]. Additionally, the width of the diffraction peaks observed in the 20–30° range in all patterns originates from the diffraction response of the Si substrate, a common feature in XRD patterns of silicon substrates [25].

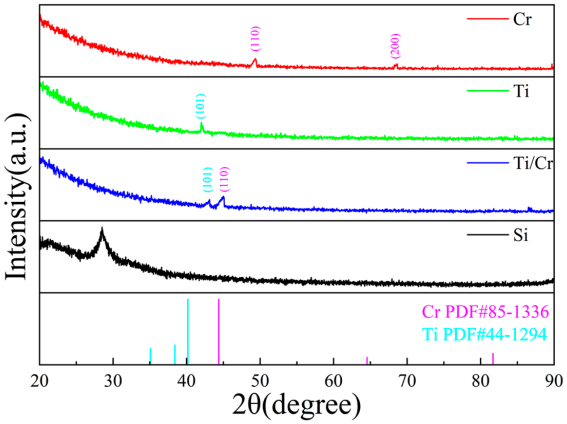


Figure 1. XRD diffraction patterns of the coatings and Si substrate.

3.2. Morphology of the Coatings

Figure 2 shows the microstructural organization of cross-sections of different coatings on silicon wafers. The thicknesses of the Cr coating, Ti coating, and Ti/Cr multilayer coating are approximately 588 nm, 94 nm, and 242 nm, respectively. This difference primarily stems from the varying deposition rates of the different target materials during the magnetron sputtering process, with the Ti target exhibiting a significantly lower deposition rate than the Cr target. Microscopic structural observations reveal that the Cr coating has a relatively loose structure with numerous pore defects visible within the coating; the Ti coating exhibits a dense columnar crystal structure. This difference primarily stems from the lower surface diffusion coefficient and higher sputtering yield of Cr atoms, leading to rapid deposition but insufficient atomic rearrangement, resulting in a loosely packed structure. In contrast, Ti atoms have higher surface mobility and stronger interatomic bonding, enabling the formation of a dense and uniform film despite the slower deposition rate [26]. The cross-sectional morphology of Ti/Cr multilayer coatings is regulated by the multilayer structure, which relatively suppresses the large-scale growth of columnar crystals while effectively bridging the pores in the Cr coating, resulting in a relatively dense and uniform columnar crystal structure.

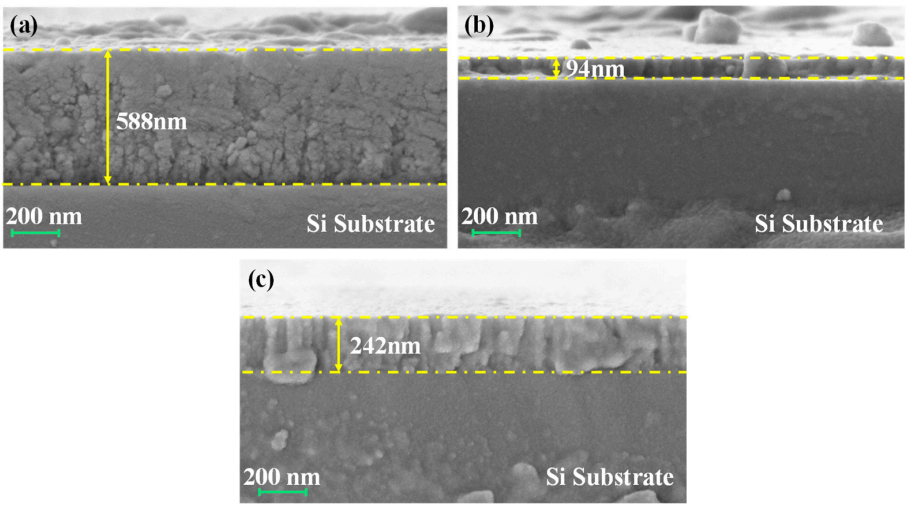


Figure 2. SEM images of coating cross-sections: (**a**)—Cr coating; (**b**)—Ti coating; (**c**)—Ti/Cr multilayer coating.

Figure 3 shows the morphological characteristics of different coatings on the aluminum substrate surface. Due to the characteristics of the direct current magnetron sputtering process, the coating surface is generally smooth, with almost no obvious particle or droplet defects [27]. The Cr coating shown in Figure 3a exhibits a typical pyramid-shaped morphology, with visible through cracks on the surface. This defect is attributed to the accumulation of internal stress caused by high-power magnetron sputtering bombardment of the Cr target material, leading to coating cracking [28]; the Ti coating shown in Figure 3b exhibits a granular structure and is the most dense; The Ti/Cr multilayer coating shown in Figure 3c also exhibits a granular morphology. Although the outermost layer is a Cr sublayer, due to the template effect [29], its growth morphology on the Ti sublayer is similar to that of the Ti coating shown in Figure 3b, both exhibiting a granular structure. However, due to the inherent properties of the Cr layer, cracks defects can still be observed on the surface of this multilayer coating.

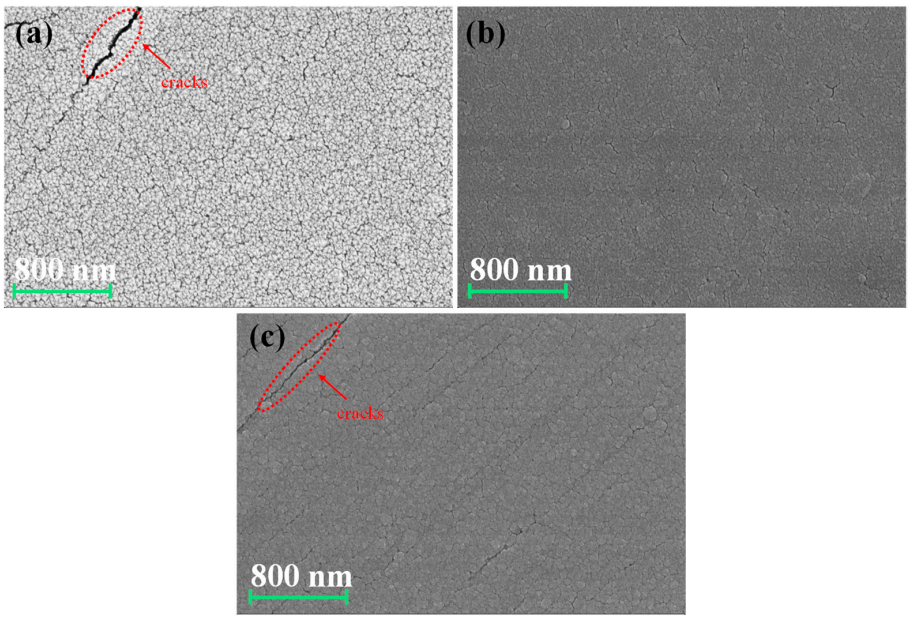


Figure 3. SEM images of the coated surfaces: (**a**)—Cr coating; (**b**)—Ti coating; (**c**)—Ti/Cr multilayer coating.

3.3. Electrochemical Properties

Figure 4 shows the open-circuit potential changes in the coated and uncoated aluminum alloy samples tested in a 3.5 wt.% NaCl solution for 1800 s. The open-circuit potential values of the coated samples were all higher than those of the uncoated aluminum alloy, indicating that the aluminum alloy had undergone surface modification through coating deposition. The open-circuit potential of the Cr coating samples decreases gradually with increasing test time and exhibits fluctuating characteristics, attributed to the penetration of the corrosion medium through defects into the substrate; the open-circuit potential of the Ti coating samples decreases gradually with increasing test time, as the Ti coating samples is too thin, shortening the corrosion medium's path [15]. In the early stages of testing, the Ti/Cr multilayer coating samples experienced only minor corrosion due to the barrier effect at the multilayer interfaces, and this resistance lasted longer than that of the Cr coating and Ti coating samples. However, when the test time reached approximately 1200 s, the open-circuit potential began to decrease, as the corrosive medium penetrated the tortuous corrosion pathways and multilayer barriers to diffuse into the substrate, causing pitting corrosion [30].

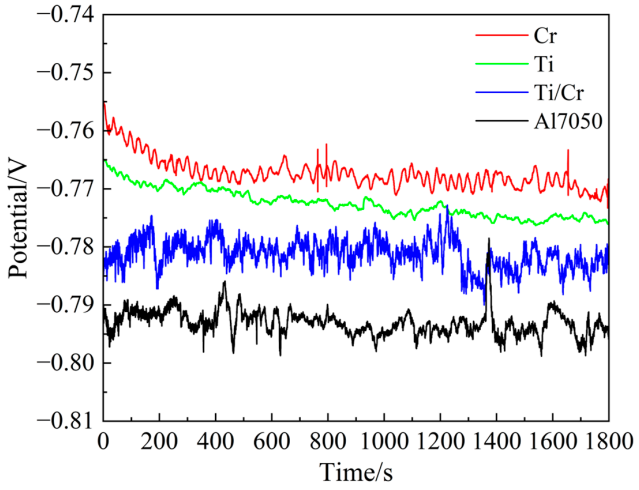


Figure 4. Open-circuit potential of substrate and coating samples.

Figure 5 shows the Potentiodynamic polarization curves of uncoated, Cr-coated, Ti-coated, and Ti/Cr multi-layer coated samples. The corrosion parameters obtained by Tafel extrapolation fitting of the polarization curves are listed in Table 1. The corrosion current density of the aluminum alloy is one to two orders of magnitude higher than that of the coated samples. Theoretically, a lower corrosion current density typically indicates higher thermodynamic stability and superior corrosion resistance of the material, which helps delay the destruction and dissolution of the passivation film [31,32]. The bare aluminum alloy exhibits pitting corrosion behavior at approximately –0.875 V, indicating that the in situ-generated Al_2O_3 passivation film on its surface has been penetrated, losing its protective function for the aluminum alloy interior [33]. Cr and Ti coatings reduced the corrosion current density of the aluminum alloy (3.46×10^{-5} A·cm^{-2}) to 9.14×10^{-6} and 8.50×10^{-7} A·cm^{-2}, respectively. This is attributed to the thermodynamically stable TiO_2 and Cr_2O_3 passivation films formed on the surface, which delay the corrosion medium's erosion of the substrate [34,35]. It is worth noting that the Cr coating exhibited significant current fluctuations within the passivation zone, which is related to its porous structure. This can cause localized delamination of the passivation film on the surface, exposing pores and forming corrosion pits, thereby leading to sudden fluctuations in corrosion current density [36]. In contrast, the corrosion current density of the Ti/Cr multilayer

coating samples further decreased to 3.83×10^{-7} A·cm^{-2}, demonstrating the best corrosion resistance performance. In addition, the polarization resistance was calculated using the Stern–Geary equation:

$$R_{p,\text{calculatedvalues}} = \frac{\beta_a \beta_c}{2.303 I_{corr}(\beta_a + \beta_c)A}$$

where β_a and β_c represent the anodic and cathodic Tafel slopes, respectively; I_{corr} denotes the corrosion current density; and A is the exposed surface area of the tested sample. This parameter reflects the difficulty of the corrosion reaction: in general, a larger $R_{p,\text{ calculated value}}$ corresponds to superior corrosion resistance of the coating [37]. As shown in Table 1, the Ti/Cr multilayer coating exhibits the highest calculated polarization resistance, reaching 12,940 Ω·cm^2.

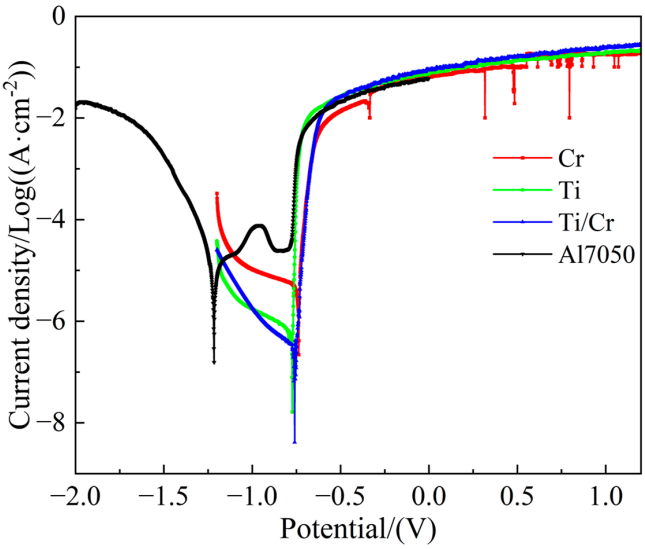


Figure 5. Potentiodynamic polarization curves of substrate and coating samples.

Table 1. Tafel fitting parameters of Potentiodynamic polarization curves.

Samples	E_{corr} (V)	I_{corr} (A·cm^{-2})	β_a (V/dec)	β_c (V/dec)	$R_{p,\text{ calculated values}}$ (Ω·cm^2)
Cr	−0.737	9.14×10^{-6}	0.06	2.48	1123
Ti	−0.773	8.50×10^{-7}	0.04	0.88	8939
Ti/Cr	−0.760	3.83×10^{-7}	0.04	0.47	12,940
Al7050	−1.216	3.46×10^{-5}	3.30	0.15	61.8

The corrosion resistance of 7050 aluminum alloy substrates and coated samples was evaluated using electrochemical impedance spectroscopy, with the test results shown in Figure 6. The aluminum alloy substrate exhibited a capacitive loop in the high-frequency region and Warburg impedance characteristics in the mid- and high-frequency regions, indicating that corrosion products had formed on the aluminum substrate surface, diffusion processes had occurred, and the substrate had been severely corroded. Therefore, subsequent corrosion resistance rankings were performed solely on the coatings [38]. The impedance spectra of each coating sample exhibited similar shapes, with a capacitive loop in the high- and medium-frequency ranges and an inductive loop in the low-frequency range. This indicates that the corrosive medium can diffuse through defects in the coating to the coating/substrate interface, triggering electrochemical reactions [39]. Generally, the larger the capacitive arc radius, the better the material's corrosion resistance [40]. The cor-

rosion resistance performance follows the following order: Cr coating < Ti coating < Ti/Cr multilayer coating.

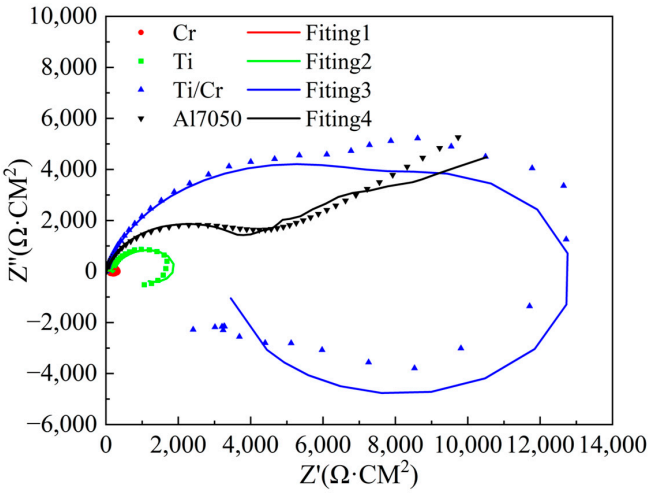


Figure 6. Nyquist plots of electrochemical impedance spectra of substrate and coating samples.

The electrochemical Bode plots of the coated samples in a 3.5 wt.% NaCl solution are shown in Figure 7. In the impedance-frequency curve, the impedance modulus values in the high-frequency and low-frequency regions, respectively, reflect the resistance of the solution and coating in the electrochemical system. The greater the difference between the impedance modulus values in the low-frequency and high-frequency regions, the higher the polarization resistance of the representative system [41]. As shown in Figure 7a, it is evident that the polarization resistance of the Ti/Cr multilayer coating is the highest, with the Ti coating exhibiting higher polarization resistance than the Cr coating. In the phase angle-frequency curve, a phase angle of −90° corresponds to an insulating layer with high resistance and low capacitance, indicating better protective performance of the coating [42]. The peak of the Ti/Cr multilayer coating is closest to −90°, followed by the Ti coating, while the Cr coating performs the worst. Additionally, phase angle peaks are observed in both the high-frequency and low-frequency regions for both Cr and Ti coatings, indicating dual-layer electrochemical behavior [43]. The time constants in the high-frequency region correspond to the capacitance characteristics of formed Cr_2O_3 and TiO_2, while the low-frequency region represents the charge transfer process between the coating and the aluminum alloy, indicating that the corrosive medium has reached the coating/substrate interface [44,45].

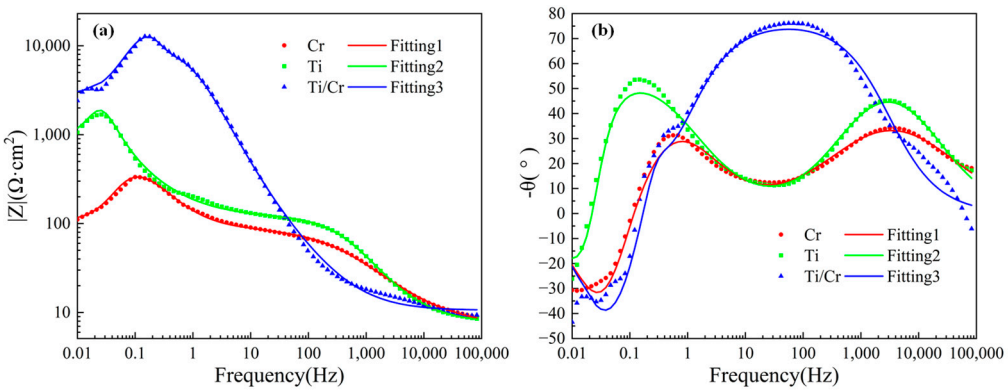


Figure 7. Bode plots of electrochemical impedance spectra of coated samples: (**a**) impedance-frequency; (**b**) phase angle-frequency.

In Figure 8a, R_s denotes the solution resistance, while R_{ct} and CPE_{dl} are connected in parallel to form the main capacitance loop, corresponding to the non-ideal capacitance of the interfacial electric double layer and the charge transfer pathways induced by defect sites in the oxide film, respectively. This path is closely related to the enrichment of intermetallic compounds, which can easily lead to localized breakdown of the passivation film and exposure of the substrate. W_1 represents the Warburg impedance, indicating the corrosion process where the corrosive medium invades the aluminum alloy substrate at low frequencies, marking an important transition in the corrosion kinetics from the diffusion-controlled stage to the diffusion-controlled stage [46]. In Figure 8b, R_s denotes the solution resistance. R_f denotes the coating resistance, CPE_f denotes the coating capacitance, and the mid-frequency capacitive loop originates from the diffusion process of the coating on the alloy surface. R_{ct} is the charge transfer resistance associated with metal oxidation reactions, while CPE_{Qdl} represents the double-layer capacitance, describing the low-frequency capacitive loop. R_L and L describe the low-frequency inductive loop, reflecting the adsorption–desorption behavior of the coating during Faraday reactions and the current oscillations triggered in the initial stage of localized corrosion, attributed to corrosion nucleation in the initial stage of localized corrosion [47,48]. The chi-squared fitting coefficients for all circuits are in the 10^{-3} order of magnitude, indicating that the equivalent circuits have good matching. The electrochemical impedance spectroscopy (EIS) fitting results for the coating samples are summarized in Table 2.

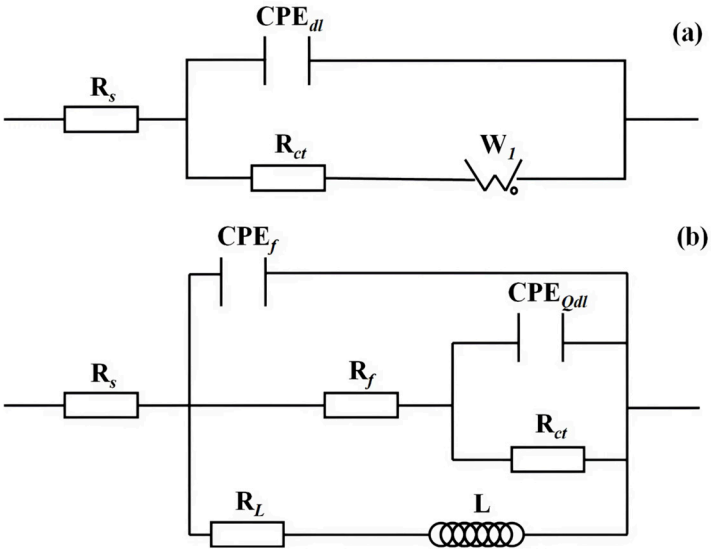


Figure 8. Equivalent circuit models used to fit the electrochemical impedance spectra of 3.5 wt% sodium chloride solutions: (**a**)—Al7050 equivalent circuit model; (**b**)—coated equivalent circuit model.

Table 2. EIS fitting results for coating samples in the equivalent circuit.

Coating Samples	R_s	CPE_f		R_f	CPE_{Qdl}		R_{ct}	R_L	L
	($\Omega \cdot cm^2$)	Y_0 ($\Omega^{-1} \cdot cm^{-2} \cdot s^n$)	n	($\Omega \cdot cm^2$)	Y_0 ($\Omega^{-1} \cdot cm^{-2} \cdot s^n$)	n	($\Omega \cdot cm^2$)	($\Omega \cdot cm^2$)	-
Cr	6.816	2.11×10^{-3}	0.614	83	9.56×10^{-5}	0.791	325	1367	1345
Ti	7.513	1.99×10^{-5}	0.759	116	1.77×10^{-3}	0.717	5571	1086	16,191
Ti/Cr	10.58	1.96×10^{-5}	0.858	10,708	1.59×10^{-4}	0.749	3100	3674	31,182

The impedance of an electrochemical system is composed of the coating resistance R_f and the charge transfer resistance R_{ct}, i.e., the polarization resistance R_p can be calculated using the formula $R_p = R_f + R_{ct}$. Additionally, the polarization resistance R_p reflects the

penetration resistance of the coating or oxide film and can be used to evaluate the protective performance of the coating or oxide film; the larger the R_p value, the stronger the corrosion resistance [49]. The R_p values for Cr coatings, Ti coatings, and Ti/Cr multilayer coatings are 408, 5687 and 13,808 $\Omega \cdot cm^2$, respectively. The corrosion resistance performance, from highest to lowest, is consistent with the results of the polarization curves.

3.4. Corrosion Morphology Analysis

Figure 9 and Table 3 show the EDS surface scan results of each sample after electrochemical corrosion testing. The Ti/Cr multilayer coating maintained its overall integrity after corrosion, with only minor corrosion traces appearing in localized areas. During the corrosion process, part of the surface Cr sublayer was consumed, exposing the Ti sublayer in localized areas. The surface element distribution was uniform, and Cl element signals were barely detected, indicating that the coating effectively blocked the penetration of the corrosive medium. In contrast, although the Ti coating has a dense structure, its thickness is relatively thin, resulting in complete exposure of the substrate during corrosion; the Cr coating, due to the presence of numerous pores, allows corrosion media to penetrate internally along defect pathways, leading to substrate exposure and corrosion. The exposed Al7050 alloy surface underwent severe corrosion, covered with extensive corrosion products, and showed significantly elevated Cl and O element contents, reflecting intense chloride ion erosion. As such, multi-layer structures demonstrate a clear advantage in enhancing coating density and corrosion resistance.

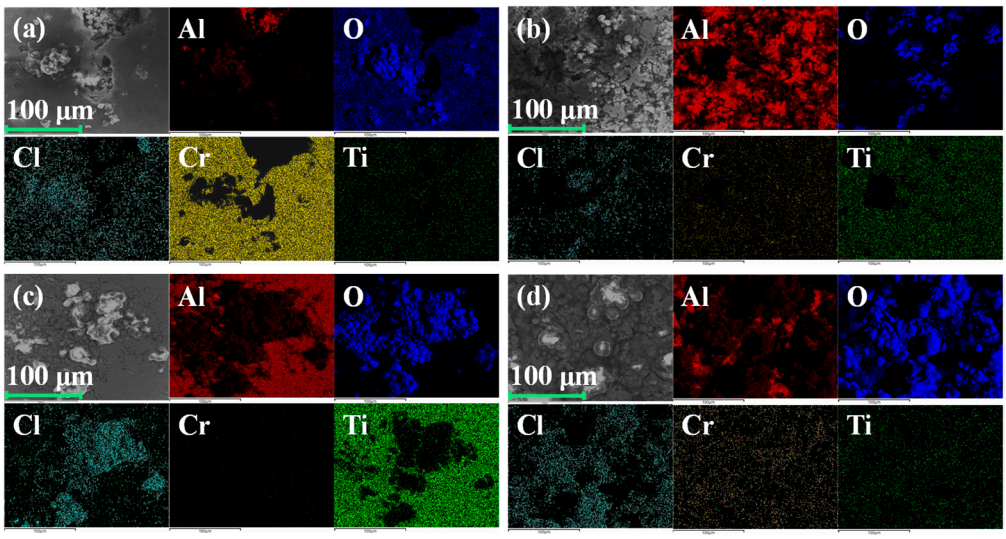


Figure 9. EDS surface analysis of (**a**) Cr; (**b**) Ti; and (**c**) Ti/Cr multilayer coatings and (**d**) Al7050 substrate after electrochemical testing.

Table 3. EDS Surface Scanning Analysis Results of the Coating and Substrate Surface After Electrochemical Testing.

Samples	Al (wt.%)	O (wt.%)	Cl (wt.%)	Cr (wt.%)	Ti (wt.%)
Cr	21.71	40.30	0.42	37.55	0.01
Ti	58.31	34.23	0.34	0.38	6.74
Ti/Cr	44.26	44.56	0.90	5.12	5.17
Al7050	36.54	60.10	3.18	0.05	0.14

4. Discussion

The corrosion resistance of coatings is influenced by a combination of factors, primarily the number of defects penetrating the thickness, the length of the corrosion path, and the

resistance to crack propagation [22]. This study systematically compared the structural characteristics and corrosion behavior of three coatings (Cr coating, Ti coating, and Ti/Cr multilayer coating), formed by a direct current magnetron sputtering process. The results indicate that corrosion resistance not only depends on the coating thickness but is also closely related to the coating's structural density, interface structure, galvanic corrosion behavior, and defect control capability. First, although the Cr coating has the greatest thickness (approximately 588 nm), it tends to form columnar crystals and a loose structure with high porosity during deposition. These structural defects provide direct pathways for corrosion media penetration. In 3.5% NaCl solution environment, Cl^- ions easily diffuse into the coating along the pores, penetrate the coating to reach the substrate, and trigger pitting corrosion. In addition, due to the potential difference between chromium (Cr) and aluminum (Al), the potential difference drives the initial corrosion process, and under the action of microelectrochemical corrosion, the aluminum substrate is more susceptible to corrosion [15]. The significant enrichment of Cl elements in the Cr coating sample shown in Figure 9a confirms this corrosion mechanism. In contrast, although the Ti coating is the thinnest (only 94 nm), it has high atomic mobility, a slow and uniform film formation process, and forms a structurally dense columnar crystal structure, thereby possessing a certain corrosion barrier capability. Although Cl signals appear after corrosion, no large-area corrosion products are observed in Figure 9b, indicating that the Ti coating can effectively delay the diffusion of the corrosion medium in the short term. However, due to the limited coating thickness, once local surface damage occurs, corrosion pathways rapidly penetrate to the substrate, thereby limiting its long-term protective performance [50]. Notably, the Ti/Cr multilayer coating demonstrates the best corrosion resistance performance. The multilayer design effectively interrupts the continuity of defects (such as pores and cracks) in the Cr sublayer, resulting in a more compact coating structure. SEM cross-sectional analysis also confirms its uniform columnar crystal structure. Each Ti/Cr interface can be regarded as a "refraction surface" for corrosion pathways, altering the direction of corrosion medium transmission and forming a "meandering diffusion mechanism," thereby significantly increasing the diffusion distance and time of corrosion pathways [51]. This mechanism is validated in the EDS of Figure 9c, where almost no Cl elements are detected penetrating into the substrate. The introduction of the Ti layer partially reduces the potential difference between the Cr layer and the Al substrate, effectively mitigating the localized anodic reaction caused by galvanic corrosion; simultaneously, since the outermost layer is Cr, the Ti layer acts as a "barrier intermediate layer" to further delay the attack process of Cl^-. Additionally, the multilayer structure facilitates crack passivation and deflection. When cracks traverse the hard-soft layer interfaces, they are often deflected or terminated due to differences in elastic modulus and crystal orientation, thereby preventing the formation of through cracks in the coating during service and enhancing the overall structural stability [52].

5. Conclusions

In this study, Cr coatings, Ti coatings, and Ti/Cr multilayer coatings were prepared on the surface of Al7050 aluminum alloy using direct current magnetron sputtering technology. The structural characteristics and corrosion resistance of these coatings were systematically investigated. The results showed that although the Cr coating had the greatest thickness, its structure was loose and contained a large number of pore defects. The Ti coating exhibited a dense structure but had the smallest thickness and was susceptible to localized corrosion penetration. In contrast, the layered structure of the Ti/Cr multilayer coating disrupts the continuity of pores in the Cr coating, effectively blocking corrosion pathways, while also increasing the overall thickness of the Ti layer, enhancing its barrier performance.

Electrochemical test results showed that the corrosion current density of the uncoated Al7050 aluminum alloy reached 3.46×10^{-5} A·cm^{-2}, with significant corrosion dissolution observed on the surface; after protection by Cr and Ti coatings, the corrosion current densities were reduced to 9.14×10^{-6} and 8.50×10^{-7} A·cm^{-2}, respectively, while the corrosion current density of the Ti/Cr multilayer coating further decreased to 3.83×10^{-7} A·cm^{-2}, demonstrating the most outstanding corrosion resistance. This performance improvement is not only attributed to the blocking effect of pore continuity in the multilayer structure but also to the Ti/Cr multilayer coating weakening the galvanic corrosion driving force between Cr and the Al7050 substrate, while extending the corrosion medium's transmission path within the Ti layer, thereby enhancing its corrosion resistance.

Further research will focus on optimizing the individual sublayer thicknesses and the number of Ti/Cr bilayers to maximize long-term corrosion protection. Specifically, investigations will explore the impact of varying sputtering parameters, such as substrate temperature and gas pressure, on the multilayer coating's microstructure, adhesion strength, and mechanical properties. The potential of incorporating corrosion inhibitors or using reactive sputtering to introduce alloying elements into the layers will also be explored to further enhance the corrosion resistance and tailor the coating properties for specific environmental conditions. Long-term exposure testing in simulated and real-world corrosive environments is crucial to validate the performance of optimized multilayer coatings and assess their suitability for industrial applications.

Author Contributions: Conceptualization, K.C. and T.H.; methodology, K.C.; validation, K.C., T.H. and A.O.; formal analysis, K.C.; investigation, K.C.; resources, T.H.; data curation, K.C., X.D. and Y.D.; writing—original draft preparation, K.C.; writing—review and editing, T.H., Y.D., P.H. and Y.W.; supervision, T.H., A.O. and C.S.; project administration, T.H. and K.C.; funding acquisition, T.H. All authors have read and agreed to the published version of the manuscript.

Funding: This research was funded by National Natural Science Foundation of China (Grant No. 52275350), International Cooperation Research Platform Construction Project of Shanghai University of Engineering Science (Grant No. 0301006), The framework of the state assignment of the Ministry of Science and Higher Education of the Russian Federation for the IMP UB RAS (theme "Structure" No. 122021000033-2).

Institutional Review Board Statement: Not applicable.

Informed Consent Statement: Not applicable.

Data Availability Statement: Data are contained within the article.

Conflicts of Interest: The authors declare no conflicts of interest.

References

1. Zhang, J.; He, T.; Du, X.; Alexey, V.; Song, M.; Chen, X. Enhanced mechanical properties in 7075 Al alloy fasteners processed by post ECAP-CU aging. *Mater. Today Commun.* **2025**, *45*, 112274. [CrossRef]
2. Jia, D.-S.; He, T.; Song, M.; Huo, Y.-M.; Hu, H.-Y. Effects of equal channel angular pressing and further cold upsetting process to the kinetics of precipitation during aging of 7050 aluminum alloy. *J. Mater. Res. Technol.* **2023**, *26*, 5126–5140. [CrossRef]
3. Berlanga-Labari, C.; Biezma-Moraleda, M.V.; Rivero, P.J. Corrosion of Cast Aluminum Alloys: A Review. *Metals* **2020**, *10*, 1384. [CrossRef]
4. Wang, G.; Sun, W.; Xu, D.; Zhang, M.; Niu, L.; Wang, Y. Effects of rare earth element content on the microstructural properties and corrosion resistance of Al-Zn alloy. *Mater. Res. Bull.* **2025**, *184*, 113227. [CrossRef]
5. Zhang, J.-J.; He, T.; Du, X.-Y.; Alexer, V.; Song, M.; Chen, X.-L.; Li, J. Effect of pre-heat treatment and subsequent ECAP-CU on microstructure and corrosion behavior of 7075 Al alloy fasteners. *J. Cent. South Univ.* **2025**, *32*, 2383–2403. [CrossRef]
6. Li, J.; He, T.; Du, X.-Y.; Vereschaka, A. Enhancing the corrosion resistance of high-strength Al-Zn-Mg-Cu alloys after equal channel angular pressing by developing retrogression and re-aging strategies. *Corros. Sci.* **2025**, *246*, 112736. [CrossRef]

7. Yan, L.; Deng, W.; Wang, N.; Xue, X.; Hua, J.; Chen, Z. Anti-Corrosion Reinforcements Using Coating Technologies—A Review. *Polymers* **2022**, *14*, 4782. [CrossRef] [PubMed]
8. Wang, Y.; He, T.; Du, X.; Vereschaka, A.; Sotova, C.; Ding, Y.; Chen, K.; Li, J.; He, P. Influence of Aluminum Alloy Substrate Temperature on Microstructure and Corrosion Resistance of Cr/Ti Bilayer Coatings. *Coatings* **2025**, *15*, 891. [CrossRef]
9. Murmu, U.K.; Roy, A.; Ghosh, A.; Eivani, A.R.; Dutta, M.; Ghosh, M. Evaluating the performance of sputter-deposited Aluminium alloy-based coatings on steel in the light of grain orientation, surface roughness, and corrosion behaviour. *Can. Metall. Q.* **2022**, *61*, 251–264. [CrossRef]
10. Han, Z.; Wang, Z.; Wang, Z.; Tan, S.; Wang, A.; Piao, Z.; Ke, P. Tailored high-temperature corrosion behavior of Cr coatings using high power impulse magnetron sputtering on ZIRLO alloys for accident-tolerant fuel application. *Surf. Coat. Technol.* **2024**, *488*, 130941. [CrossRef]
11. Zhang, M.; Wang, L.; Wang, Z.; Cheng, Y.; Ma, G.; Tan, S.; Ke, P.; Wang, A. Oxygen-driven shell-like microstructure: A pathway to high-performance PVD Cr coatings for metal protection. *npj Mater. Degrad.* **2025**, *9*, 51. [CrossRef]
12. Kuo, C.-C.; Lin, C.-H.; Lin, Y.-T.; Chang, J.-T. Effects of Cathode Voltage Pulse Width in High Power Impulse Magnetron Sputtering on the Deposited Chromium Thin Films. *Coatings* **2020**, *10*, 542. [CrossRef]
13. Daroonparvar, M.; Kasar, A.K.; Farooq Khan, M.U.; Menezes, P.L.; Kay, C.M.; Misra, M.; Gupta, R.K. Improvement of Wear, Pitting Corrosion Resistance and Repassivation Ability of Mg-Based Alloys Using High Pressure Cold Sprayed (HPCS) Commercially Pure-Titanium Coatings. *Coatings* **2021**, *11*, 57. [CrossRef]
14. Sun, J.; Han, Y.; Cui, K. Innovative fabrication of porous titanium coating on titanium by cold spraying and vacuum sintering. *Mater. Lett.* **2008**, *62*, 3623–3625. [CrossRef]
15. Zhang, D.; Wei, B.; Wu, Z.; Qi, Z.; Wang, Z. A comparative study on the corrosion behaviour of Al, Ti, Zr and Hf metallic coatings deposited on AZ91D magnesium alloys. *Surf. Coat. Technol.* **2016**, *303*, 94–102. [CrossRef]
16. Yoon, H.W.; Choi, Y.; Yeo, K.H.; Kim, S.G.; Cho, Y.K. Chromium Coatings Applied to Zr Alloy Claddings by Cathodic Arc Ion Plating: Effect of Nitrogen Inclusion on Limiting Columnar Defects. *Adv. Eng. Mater.* **2024**, *26*, 2400804. [CrossRef]
17. Panjan, P.; Drnovšek, A.; Gselman, P.; Čekada, M.; Panjan, M.; Bončina, T.; Kek Merl, D. Influence of Growth Defects on the Corrosion Resistance of Sputter-Deposited TiAlN Hard Coatings. *Coatings* **2019**, *9*, 511. [CrossRef]
18. Pogrebnjak, A.D.; Lisovenko, M.A.; Turlybekuly, A.; Buranich, V.V. Protective coatings with nanoscale multilayer architecture: Current state and main trends. *Phys.-Uspekhi* **2021**, *64*, 253–279. [CrossRef]
19. Liu, Z.X.; Li, Y.; Xie, X.H.; Qin, J.; Wang, Y. The tribo-corrosion behavior of monolayer VN and multilayer VN/C hard coatings under simulated seawater. *Ceram. Int.* **2021**, *47*, 25655–25663. [CrossRef]
20. Çomaklı, O. Improved structural, mechanical, corrosion and tribocorrosion properties of Ti45Nb alloys by TiN, TiAlN monolayers, and TiAlN/TiN multilayer ceramic films. *Ceram. Int.* **2021**, *47*, 4149–4156. [CrossRef]
21. Xie, W.; Zhao, Y.; Chen, S.; Liao, B.; Zhang, S.; Hua, Q.; He, G. Corrosion resistance of AlN monolayer and Al/AlN multilayer deposited by filtered cathodic vacuum arc. *Thin Solid Films* **2023**, *772*, 139762. [CrossRef]
22. Chen, K.; He, T.; Du, X.; Vereschaka, A.; Sotova, C.; Ding, Y.; Li, J. Corrosion Resistance of Ti/Cr Gradient Modulation Period Nanomultilayer Coatings Prepared by Magnetron Sputtering on 7050 Aluminum Alloy. *Inorganics* **2025**, *13*, 242. [CrossRef]
23. Pereira, J.N.; Ott, V.; Afonso, C.R.M.; de Sousa Malafaia, A.M.; Stüber, M.; Greiner, C.; Pinto, H.C. Influence of multilayer nanoarchitecture on phase transformations in the Ti-Cr-Zr system. *Surf. Coat. Technol.* **2024**, *477*, 130369. [CrossRef]
24. Shi, W.; Peng, J.; Xu, Z.; Shen, Q.; Wang, C. Effect of Power on Structural and Mechanical Properties of DC Magnetron Sputtered Cr Coatings. *Metals* **2023**, *13*, 691. [CrossRef]
25. Mutlak, F.A.H.; Taha, A.B.; Nayef, U.M. Synthesis and Characterization of SnO_2 on Porous Silicon for Photoconversion. *Silicon* **2017**, *10*, 967–974. [CrossRef]
26. Samuelsson, M.; Lundin, D.; Jensen, J.; Raadu, M.A.; Gudmundsson, J.T.; Helmersson, U. On the film density using high power impulse magnetron sputtering. *Surf. Coat. Technol.* **2010**, *205*, 591–596. [CrossRef]
27. Xu, Y.; Li, Y.; Meng, F.; Huang, F. Microstructure and multifunctionality of a 10-μm-thick dense yet smooth Cr(C) coating prepared by low-temperature magnetron sputtering. *Surf. Coat. Technol.* **2022**, *435*, 128255. [CrossRef]
28. Sidelev, D.V.; Bleykher, G.A.; Krivobokov, V.P.; Koishybayeva, Z. High-rate magnetron sputtering with hot target. *Surf. Coat. Technol.* **2016**, *308*, 168–173. [CrossRef]
29. Sun, X.; Chen, L.; Zhou, J. Structure, mechanical and thermal properties of TiAlBN/TiAlN multilayers. *Surf. Coat. Technol.* **2022**, *441*, 128512. [CrossRef]
30. Mohan Kumar, G.; Singh, A.P.; Anupindi, S.; Srivastava, C. Effect of molybdenum partitioning induced lattice strain and surface oxide chemistry on hydrogen permeation and corrosion behavior of Co-Mo coatings. *J. Mater. Sci.* **2025**, *60*, 4764–4787. [CrossRef]
31. He, T.; Valery, Z.; Vereschaka, A.; Keshin, A.; Huo, Y.; Milovich, F.; Sotova, C.; Seleznev, A. Influence of niobium and hafnium doping on the wear and corrosion resistance of coatings based on ZrN. *J. Mater. Res. Technol.* **2023**, *27*, 6386–6399. [CrossRef]
32. Li, J.; He, T.; Du, X.-Y.; Vereschaka, A.; Zhang, J.-J. Regulating hardness homogeneity and corrosion resistance of Al-Zn-Mg-Cu alloy via ECAP combined with inter-pass aging. *Mater. Charact.* **2024**, *218*, 114489. [CrossRef]

33. Natishan, P.M.; O'Grady, W.E. Chloride Ion Interactions with Oxide-Covered Aluminum Leading to Pitting Corrosion: A Review. *J. Electrochem. Soc.* **2014**, *161*, C421–C432. [CrossRef]
34. Inman, S.B.; Sur, D.; Han, J.; Ogle, K.; Scully, J.R. Corrosion behavior of a compositionally complex alloy utilizing simultaneous Al, Cr, and Ti passivation. *Corros. Sci.* **2023**, *217*, 111138. [CrossRef]
35. Kosari Mehr, A.; Kosari Mehr, A.; Babaei, R. Performance of reactively co-sputtered titanium chromium nitride films in artificial saliva: Corrosion protection and reduction in the release of potentially toxic elements. *Surf. Coat. Technol.* **2021**, *427*, 127855. [CrossRef]
36. Peng, S.; Xu, J.; Li, Z.; Jiang, S.; Xie, Z.-H.; Munroe, P. Electrochemical noise analysis of cavitation erosion corrosion resistance of NbC nanocrystalline coating in a 3.5 wt% NaCl solution. *Surf. Coat. Technol.* **2021**, *415*, 127133. [CrossRef]
37. Hacıibrahimoğlu, M.; Bedir, M.; Yavuz, A. Structural and Corrosion Study of Uncoated and Zn-Cu Coated Magnesium-Based Alloy. *Metals* **2016**, *6*, 322. [CrossRef]
38. Won, S.; Seo, B.; Park, J.M.; Kim, H.K.; Song, K.H.; Min, S.-H.; Ha, T.K.; Park, K. Corrosion behaviors of friction welded dissimilar aluminum alloys. *Mater. Charact.* **2018**, *144*, 652–660. [CrossRef]
39. Li, S.; Wei, H.; Zhao, X.; Tang, Y.; Zuo, Y. Failure behavior and life prediction of solvent-free epoxy coatings based on impedance spectroscopy. *Electrochim. Acta* **2024**, *492*, 144349. [CrossRef]
40. Ding, Y.; He, T.; Du, X.; Vereschaka, A.; Sotova, C.; Chen, K.; Li, J.; Wang, Y.; He, P. Effect of Buffer Layer Type on the Mechanical Properties and Corrosion Resistance of Magnetron Sputtered Cr Coatings on 7050 Al Alloy. *Coatings* **2025**, *15*, 803. [CrossRef]
41. Yang, Z.; Wang, R.-Q.; Liu, C.; Wu, Y.-K.; Wang, D.-D.; Liu, X.-T.; Zhang, X.-Z.; Wu, G.-R.; Shen, D.-J. The Electrochemical Corrosion Behavior of Plasma Electrolytic Oxidation Coatings Fabricated on Aluminum in Silicate Electrolyte. *J. Mater. Eng. Perform.* **2019**, *28*, 3652–3660. [CrossRef]
42. Cui, X.-J.; Ning, C.-M.; Shang, L.-L.; Zhang, G.-A.; Liu, X.-Q. Structure and Anticorrosion, Friction, and Wear Characteristics of Pure Diamond-Like Carbon (DLC), Cr-DLC, and Cr-H-DLC Films on AZ91D Mg Alloy. *J. Mater. Eng. Perform.* **2019**, *28*, 1213–1225. [CrossRef]
43. Ko, J.S.; Lai, C.H.; Long, J.W.; Rolison, D.R.; Dunn, B.; Nelson Weker, J. Differentiating Double-Layer, Psuedocapacitance, and Battery-like Mechanisms by Analyzing Impedance Measurements in Three Dimensions. *ACS Appl. Mater. Interfaces* **2020**, *12*, 14071–14078. [CrossRef] [PubMed]
44. Mahdavian, M.; Attar, M.M. Another approach in analysis of paint coatings with EIS measurement: Phase angle at high frequencies. *Corros. Sci.* **2006**, *48*, 4152–4157. [CrossRef]
45. Martinez, S.; Šoić, I.; Špada, V. Unified equivalent circuit of dielectric permittivity and porous coating formalisms for EIS probing of thick industrial grade coatings. *Prog. Org. Coat.* **2021**, *153*, 106155. [CrossRef]
46. Seechurn, Y.; Wharton, J.A.; Surnam, B.Y.R. Mechanistic modelling of atmospheric corrosion of carbon steel in Port-Louis by electrochemical characterisation of rust layers. *Mater. Chem. Phys.* **2022**, *291*, 126694. [CrossRef]
47. Li, B.; Li, D.; Xia, W.; Zhang, W. Synthesis and characterization of a novel Zn-Ni and Zn-Ni/Si3N4 composite coating by pulse electrodeposition. *Appl. Surf. Sci.* **2018**, *458*, 665–677. [CrossRef]
48. Mouanga, M.; Puiggali, M.; Devos, O. EIS and LEIS investigation of aging low carbon steel with Zn–Ni coating. *Electrochim. Acta* **2013**, *106*, 82–90. [CrossRef]
49. Khazeni, D.; Saremi, M.; Soltani, R. Development of HA-CNTs composite coating on AZ31 Magnesium alloy by cathodic electrodeposition. Part 2: Electrochemical and in-vitro behavior. *Ceram. Int.* **2019**, *45*, 11186–11194. [CrossRef]
50. Abdeen, D.H.; El Hachach, M.; Koc, M.; Atieh, M.A. A Review on the Corrosion Behaviour of Nanocoatings on Metallic Substrates. *Materials* **2019**, *12*, 210. [CrossRef]
51. He, Q.; Liu, D.; Zhou, Y.; Sun, T.-Y.; Huang, L.-F. Nitride coatings for environmental barriers: The key microscopic mechanisms and momentous applications of first-principles calculations. *Surf. Sci. Technol.* **2024**, *2*, 24. [CrossRef]
52. Li, Q.; Cui, X.; Jing, Y.; Xu, W.; Wang, Y.; Chen, Z.; Zhang, Z.; Fang, Y.; Shang, T.; Jin, G. Multi-interface modification induced crack deflection behavior and enhanced fracture resistance in thermal barrier coatings. *J. Alloys Compd.* **2025**, *1031*, 181027. [CrossRef]

Disclaimer/Publisher's Note: The statements, opinions and data contained in all publications are solely those of the individual author(s) and contributor(s) and not of MDPI and/or the editor(s). MDPI and/or the editor(s) disclaim responsibility for any injury to people or property resulting from any ideas, methods, instructions or products referred to in the content.